Sulfidation of CoMoP catalysts: genesis of the Mo multiscale organization from oxides to sulfides

Candice Cottrez, Severine Humbert, Anne-Sophie Gay, Elodie Devers, Frédéric De Geuser, Christèle Legens, Xavier Carrier, Alexandra Chaumonnot

ChemCatChem

The European Society Journal for Catalysis

Chemistry Europe

European Chemical Societies Publishing

Supported by

GECATS GERMAN CATALYSIS SOCIETY

Accepted Article

Title: Sulfidation of CoMoP catalysts: genesis of the Mo multiscale organization from oxides to sulfides

Authors: Candice Cottrez, Severine Humbert, Anne-Sophie Gay, Elodie Devers, Frederic De Geuser, Christèle Legens, Xavier Carrier, and Alexandra Chaumonnot

To be cited as: *ChemCatChem* **2025**, e202401670

Link to VoR: https://doi.org/10.1002/cctc.202401670

WILEY VCH

10.1002/cctc.202401670

WILEY VCH

RESEARCH ARTICLE

Sulfidation of CoMoP catalysts: genesis of the Mo multiscale organization from oxides to sulfides

Candice Cottrez[a], Séverine Humbert[a], Anne-Sophie Gay*[a], Elodie Devers*[a], Frédéric De Geuser[b], Christèle Legens[a], Xavier Carrier[c] and Alexandra Chaumonnot[a]

[a] Dr. Candice Cottrez, Dr. Séverine Humbert, Dr. Anne-Sophie Gay, Dr. Elodie Devers, Dr. Christèle Legens, Dr. Alexandra Chaumonnot
IFP Energies Nouvelles
Rond-Point de l'échangeur de Solaize, BP3, 69360 Solaize, France
* Corresponding authors: anne-sophie.gay@ifpen.fr; elodie.devers@ifpen.fr

[b] Dr. Frédéric de Geuser
Univ Grenoble Alpes, CNRS, Grenoble INP, Lab SIMaP
F-38000 Grenoble, France

[c] Dr. Xavier Carrier
Sorbonne Université, CNRS, Laboratoire de Réactivité de Surface, LRS
F-75005, PARIS, France

Supporting information for this article is given via a link at the end of the document.

Abstract: MoS_2 active phase found in $CoMoP/Al_2O_3$ catalysts can be described as a multiscale Mo organization with MoS_2 slabs and slab aggregates. The aim of this paper is to understand how such multiscale organization is formed from the oxide initial state. Sulfidation of two catalysts impregnated with 26 %wt MoO_3, one dried, the other one freeze-dried, has been followed *ex situ* by EXAFS, XPS and ASAXS. Initially, two types of Mo oxide precursors are present on the support such as dispersed MoO_4^{2-} species and oxide aggregates constituted of heteropolyanions, polymolybdates and $H_6AlMo_6O_{24}^{6-}$ Anderson HPA ($AlMo_6$). A 3-step genesis is highlighted during the sulfidation regardless of the catalyst: i) Polymeric molybdenum species depolymerizes into MoO_4^{2-} entities from RT to 240°C, ii) MoO_4^{2-} is preferentially sulfided compared to other entities and slab aggregates sulfidation is delayed, probably in the presence of important MoO_4^{2-} amount, iii) restructuration of the slabs within slab aggregates occurs during sulfidation of the latter and leads to their expansion. The drying method (drying or freeze-drying) influences the kinetics of this 3-steps genesis. As the freeze-dried catalyst presents more $AlMo_6$ and thus MoO_4^{2-}, a late restructuration within aggregates leads to larger ones. Initial speciation of the catalysts determines the final Mo multiscale organization.

Introduction

While renewable energies gain importance, demand for clean fossil fuels continues to grow [1]. High fuel demand and stringent pollution control standards (*i.e.* in Europe, less than 10 ppm sulfur is required in automotive fuels) mean that hydrodesulfurization (HDS) catalysts have to be ever more intrinsically efficient.

Such catalysts are mainly composed of a metal sulfide active phase (group VIB, *e.g.* Mo or W), promoted by a dopant (group VIII, *e.g.* Co or Ni) to enhance catalytic activity [2]. This phase is dispersed within the porosity of an oxide support such as γ-Al_2O_3. Catalytic activity is due to the formation of mixed sites CoMoS, present at the edges of MoS_2 slabs [3, 4]. These cobalt-promoted MoS_2 slabs are usually found as more or less stacked, with an average length of around 2 to 4 nm [5, 6]. However, recent studies have demonstrated that it is also relevant to consider the active phase as a multiscale organization [7, 8]. At a larger scale, slab aggregates of the order of a dozen nanometers in width exist. A slab aggregate is made up of entangled slabs resulting from the aggregation of slabs and it has been proven to be detrimental for the HDS activity. At a smaller scale, presence of ultradispersed MoO_xS_y or MoS_x nanoclusters have also been raised and might be involved in catalytic activity [9–13].

Commonly, HDS catalysts are prepared by a 3-step method prior to activation by sulfidation [6, 14]: i) Mo and Co oxide precursors dissolved in an aqueous solution are impregnated by incipient wetness impregnation on the support, ii) an ageing step is carried out to let the metals diffuse within the support porosity, iii) then a drying step is finally applied to remove the solvent.

There are two main kinds of studies in literature trying to relate the synthesis conditions to the state of the active phase. The first type of study investigates the influence of synthesis parameters on the morphology of MoS_2 slabs. Thus, surface reactivity [15–17] and textural properties [18–20] of the support, impregnation solution properties such as viscosity, pH [6, 21, 22], Mo loading [23–25] and speciation [22, 26, 27] are the numerous parameters that can actually drive the MoS_2 slabs size, stacking, promotion rate, sulfidation rate. In the same context, it has also been shown that synthesis conditions, such as the use of organic additives, can induce different states of slab aggregation [7]. The same applies to drying conditions.

Our previous work [8] studied different drying processes such as evaporation (*i.e.* conventional drying taking place in an oven) and sublimation by freeze-drying. Freeze-drying fixes the system after ageing and leads to large slab aggregates, whereas during conventional drying a fragmentation of aggregates occurs, probably due to the redistribution of metals. Besides, it was

proven that slab aggregates are detrimental for the intrinsic catalytic activity while the presence of a high proportion of small isolated/stacked slabs is beneficial.

The second type of study is more focused on describing the oxide state. Before sulfidation, different Mo species can be distinguished and be grouped into two families: isopolyanions such as mono- or polymolybdates (PM), and heteropolyanions (HPA). The latter can also be subdivided in 2 groups: on one side the Stranderg, Dawson or Keggin HPA which are phosphorus-containing HPA (P-HPA), and on the other side the $H_6AlMo_6O_{24}^{3-}$ Anderson HPA ($AlMo_6$). P-HPA have been shown since decades [2, 28] to be beneficial for the catalytic activity as they improve the Mo dispersion [22, 29]. $AlMo_6$ (Anderson HPA) is formed by Al_2O_3 support dissolution during impregnation and ageing [30], and shows a low solubility that leads to its precipitation [6].
Severity of drying [25, 27, 31, 32] (*e.g.* time, temperature, drying ramp) also appears to be a determining factor as equilibrium is modified due to solvent evaporation. The drying step induces a strong change in speciation of Mo species as it has been recently demonstrated by Barata et al. [33]. Strandberg, Anderson and Dawson HPAs found at the end of the maturation stage are indeed transformed into lacunary Keggin HPA, octa- and monomolybdates. Drying also induces particles redistribution and precipitation within the support [14].
Despite this abundant literature, the relationship between Mo speciation in the oxide state and the morphology of the active phase after sulfidation is not obvious, as the transition mechanism remains rather unclear.
Sulfidation mechanism to obtain the MoS_2 active phase has been deeply investigated the past decades. First studies [34–36] following the gas-phase sulfidation mechanism for Mo/Al_2O_3 catalyst by *in-situ* Raman revealed the presence of MoO_xS_y oxysulfides as intermediate species. Afterwards, Payen et al. [12] reassigned the Raman lines and postulated that not only one, but two intermediate species exist during gas-phase sulfidation : oxidic precursors are first converted into MoO_xS_y species, then to MoS_3 before finally forming the MoS_2 active phase. Such mechanism has been confirmed more recently by Rochet et al. [13] with a gas-phase sulfidation of Mo/Al_2O_3 catalysts followed by *in-situ* EXAFS. However, in the case of promoted catalyst ($CoMo/Al_2O_3$), only one intermediate precursor such as MoS_3 is found [13]. This highlights the role of the oxide precursors on the sulfidation mechanism. However, gas-phase versus liquid-phase sulfidation is another variable. In a recent work, Lesage et al. [37] followed the speciation of Mo particles during liquid-phase sulfidation ($DMDS/H_2$) by quick-XAS. They showed the depolymerization of Mo oxide species into smaller ones at 80°C. Then, once the DMDS has decomposed at around 230°C, these new and smaller Mo oxide species are transformed into MoO_xS_y species, then MoS_x species (MoS_3) and finally MoS_2 particles, which is similar as the gas sulfidation mechanism developed by Payen et al. [12].
All these previous studies provide key information to understand the sulfidation mechanism based on the speciation of Mo species but usually do not provide evidence for the morphological evolution of the active phase. Rare studies have suggested mechanisms for the formation of stacked MoS_2 slabs from the oxide precursors. Hansen et al. [38] followed the gas-phase sulfidation (10% H_2S/H_2) of $MoO_3/MgAl_2O_4$ catalysts by TEM *in situ*. They discussed three possible mechanisms: the "layer-on-layer", which involves the growth of isolated slabs which then migrate and stack on top of each other's, the "layer-by-layer" where a new slab is nucleated on an existing well-formed mono-slab and the "layer-and-layer", where small, stacked slabs coalesce with other small stacked slabs to form new, longer slabs. They showed that unstable and mobile species MoO_xS_y obtained by sulfidation of MoO_3 particles nucleate and grow as MoS_2 nanoparticles through a "layer-by-layer" mechanism. Van Haandel et al. [39] proposed a different mechanism by following the activation by gas and liquid-phase sulfidation with a combined XAS/SAXS *in situ* study of a 10 wt% Mo catalyst supported on Al_2O_3 and additivated by citric acid (CA). Under gas-phase sulfidation, they firstly observed an aggregation step of MoS_x precursors which then coalesce to form stacked MoS_2 slabs. In the case of liquid-sulfidation, they observed only the crystallization stage: the formation of MoS_x domains is not visible. However, these mechanisms attempt to understand the formation of stacked MoS_2 slabs as a unique Mo organization. They do not consider the existence of a MoS_2 aggregated phase.

The genesis of multiscale active phase organizations (*i.e.* simultaneous presence of Mo nanoclusters, MoS_2 stacked/isolated slabs and MoS_2 slabs aggregates) has never been investigated in detailed yet. Hence, the influence of the speciation, organization and morphology of oxide precursor species on the final multiscale organization of the sulfide active phase is still to be understood. The aim of this paper is to give new insights on the genesis of both isolated slabs and aggregates in the sulfide catalyst from synthesis to sulfidation in order to understand which initial parameters are key to drive the muti-scale active phase organization.
Regarding these goals, we have selected two highly loaded catalysts containing 26 wt% MoO_3 from a previous study [8]. The first catalyst was aged after impregnation and conventionally dried and the other one was aged and freeze-dried. Key sulfidation temperatures (165°C, 250°C, 300°C and 350°C) have been chosen with respect to a previous work [37] to follow the transition of the oxide Mo species into sulfide ones. To obtain both speciation and morphological information about Mo entities during sulfidation, each catalyst has been characterized at each step of the activation by XPS and ASAXS, while initial oxide catalyst precursors have also been characterized by EXAFS.

Experimental section

Catalysts preparation

Two catalysts (A_D and A_FD) [8] were prepared by incipient wetness impregnation (IWI) of mesoporous γ-Al_2O_3 trilobal extrudates (surface area: 273 m²/g, porous volume (P/P_0 max): 0.75 ml/g) with an aqueous solution of MoO_3 (Climax Molybdenum, purity: 100%), $Co(OH)_2$ (AXENS, purity: 98%) and H_3PO_4 (VWR, purity: 98%). The molybdenum content was 26 wt% MoO_3, with

P/Mo and Co/Mo molar ratios of 0.27 and 0.40 respectively. The catalysts were aged (A) overnight at room temperature in a water-saturated atmosphere and then dried (D) in a stagnant air oven at 120°C for 5h, or freeze-dried (FD) in a freeze-dryer at -60°C for 20h. In the freeze-drying case, the catalyst was first dipped into liquid nitrogen to freeze it. The oxide catalyst precursors are named “A_D_ox” and “A_FD_ox” regarding the drying step applied.

Sulfidation was carried out using a Flowrence fixed bed reactor (Avantium) containing 16 parallel reactors. The feed used was composed of a mixture of dimethyldisulfide (DMDS, 5.9 wt%), toluene (20 wt%) and cyclohexane (74.1 wt%). The hydrogen to feed volume ratio (H_2/HC) was 450 NL/L, the liquid hourly space velocity (LHSV) was 4 h^{-1}, and the total pressure was 60 bar. The following sulfidation temperatures have been selected based on the results presented by Lesage et al. [29]: 165, 250, 300 and 350°C. During *in situ* sulfidation, target sulfidation temperatures were reached from room temperature (RT) with a ramp of 2 °C/min. Once the target temperature was reached, the reactors were cooled down. These sulfided catalysts are named “A_D_x” or “A_FD_x”, with x the sulfidation temperature applied (*e.g.* 165, 250, 300 or 350°C). They were kept in a glovebox under inert atmosphere before characterization.

For some catalysts, once the final sulfidation temperature at 350°C was reached, without aforementioned intermediate sulfidation temperatures, the temperature was maintained for a 6-h plateau where the LSVH was turned down at 2 h^{-1}. Those final catalysts are named “A_D” and “A_FD”. The entire nomenclature has been summarized in Table 1.

Table 1. Catalysts nomenclature and their synthesis parameters associated.

Sample	Drying step	Sulfidation temperature (°C)	Sulfidation duration (min)
A_D_ox	Drying	0	/
A_D_165	Drying	165	70
A_D_250	Drying	250	113
A_D_300	Drying	300	138
A_D_350	Drying	350	163
A_D	Drying	350	493
A_FD_ox	Freeze-drying	0	/
A_FD_165	Freeze-drying	165	70
A_FD_250	Freeze-drying	250	113
A_FD_300	Freeze-drying	300	138
A_FD_350	Freeze-drying	350	163
A_FD	Freeze-drying	350	493

Characterizations

Extended X-ray Absorption Fine Structure (EXAFS)

EXAFS data were collected at the Mo K-edge (20 keV) on ROCK beamline at SOLEIL synchrotron on the dried A_D_ox and freeze-dried A_FD_ox shaped catalyst precursors. The EXAFS spectra are used to identify and quantify the Mo oxide species, according to the methodology initially developed on crushed samples [29] and then successfully declined on integral extrudates [33]. For that, the catalysts are cut with a maximum length of 1.5 mm with faces as flat as possible to optimize the homogeneity of the transmitted signal, and then bonded with Kapton tape to a PEEK sample holder. The transmitted signal is then measured at the center of the extrudate over a 300 µm x 300 µm region as well as on a lobe to check the homogeneity of the impregnation respective to Mo speciation.

For each sample, an average of around 1800 spectra is taken to ensure a good signal-to-noise ratio. Extraction of EXAFS spectra were normalized using the "normal_gui" interface developed on the ROCK beamline at the SOLEIL synchrotron [29]. Calibrated spectra acquired every 500 msec were averaged using Athena(D) Software to obtain a better signal-to-noise ratio.

Mo speciation is obtained by linear combination fitting of the EXAFS spectra thanks to an existing Mo species library, done with Matlab using the "MAthena" code available for users on the synchrotron ROCK beamline.

Detailed Mo speciation of the oxide catalysts precursors are then obtained and reported in Figure A.1 (*cf.* Appendix A). However, in the present case, the choice has been made to group the Mo oxide precursors into 4 groups as it is reported in Table 2.

Table 2. Summary of Mo species present in CoMoP catalysts precursors and measurable by EXAFS technique.

Group	Mo species	Empirical formula
P-Heteropolyanions (P-HPA)	Keggin HPA	$H_xPMo_{12}O_{40}^{(3-x)-}$
	Lacunary Keggin HPA	$H_xPMo_{11}O_{39}^{(7-x)-}$
	Substituted Keggin HPA	$H_xPCoMo_{11}O_{40}^{(7-x)-}$
	Monomer Dawson HPA	$H_xPMo_9O_{34}^{(9-x)-}$
	Dimer Dawson HPA	$H_xP_2Mo_{18}O_{62}^{(6-x)-}$
	Strandberg HPA	$H_xP_2Mo_5O_{23}^{(6-x)-}$
Polymolybdates (PM)	Pentamolybdate	$H_xMo_5O_{17}^{(4-x)-}$
	Heptamolybdate	$H_xMo_7O_{24}^{(6-x)-}$
	Octamolybdate	$H_xMo_8O_{26}^{(4-x)-}$
Monomolybdates (MM)	Monomolybdates	MoO_4^{2-}
$AlMo_6$	Anderson HPA	$H_6AlMo_6O_{24}^{3-}$

X-ray Powder Diffraction (DRX)

XRD measurements were recorded on crushed catalysts precursors and were performed on a PANalytical X'Pert Pro diffractometer equipped with Cu $K\alpha_1$ source radiation, at a wavelength of 1.5406 Å and in the range of 2Θ = 5-72°.

Raman spectroscopy

Raman spectroscopy characterization of the oxide catalysts precursors was performed with a Renishaw Qontor spectrometer at 532 nm. The catalyst was placed on a glass microscope slide for the analysis. Raman spectra were acquired between 200 and 1100 cm^{-1} with a x50 objective, and a wavenumber accuracy of around 1.3 cm^{-1}. The laser power used was 2 to 3 mW with an exposure time of between 10 s and 50 s.

X-ray Photoelectron Spectroscopy (XPS)

To avoid partial reoxidation of the sulfide catalysts, XPS sampling was performed under an argon atmosphere in a glove box connected to the spectrometer, with controlled water and oxygen levels. The samples were ground and pressed onto an indium foil that was attached to the sample holder with a double-sided carbon tape and then moved directly into the analysis chamber without exposure to air. Spectra acquisition was carried out on a Kratos Axis Ultra spectrometer (Kratos Analytical, U. K.) equipped with a 128-channel delay line detector, a monochromatic Al Kα source (1486.6 eV) and a hemispherical analyzer. Measurements in the analysis chamber were carried out under high vacuum (around 10^{-9} torr) at RT. The Co 2p, Mo 3d, P 2p, S 2s, S 2p and Al 2p high resolution spectra were recorded at a passing energy of 20 eV and referenced to the C 1s main peak at 284.6 eV admitted as carbon contamination.

XPS is a powerful technique to address the chemical speciation of surface atoms, thus, contributions of different Mo, Co and S oxidation states relative to different species were extracted [40]. Areas of the corresponding peaks were integrated via Plug Im! [41], a homemade software, and corrected by the relative sensitivity factors given by the manufacturer to obtain a relative atomic concentration of the species.

Concerning molybdenum speciation, three species such as Mo(VI), Mo(V) and Mo(IV) corresponding respectively to oxide phase, oxysulfides, and MoS_2 were identified regarding the respective binding energy of the Mo 3d peaks. Decomposition of the peaks is reported in Figure D.1 and Table D.1 (Supporting information). The MoS_2 relative atomic percentage also corresponds to the Mo sulfidation rate *%MoS_2* with a relative uncertainty of about 3.4 %. The Mo/Al surface atomic ratio permits to quantify the Mo dispersion and has a relative uncertainty of 3.8 %.

The decomposion of Co 2p peaks is reported in Figure D.2 and Table D.2 (Supporting information). Similarly the cobalt signal can be decomposed into 3 contributions: i) an oxide phase such as CoO (*e.g.* Co(II)), ii) a sulfide phase (*e.g.* Co_9S_8 or CoS_2, noted CoS species), and iii) a proportion of Co involved as a promotor of MoS_2 slabs called CoMoS. The CoMoS relative atomic percentage is considered as the promotion rate *%CoMoS*. Its relative uncertainty is about 11 %.

HR STEM-HAADF

The sulfide catalysts were crushed and dry deposited on a holey carbon copper grid. Measurements were performed on a TEM JEOL NeoARM 200F operated at 200 kV in high resolution with a STEM HAADF Gatan detector. Image resolution is about 78 pm.

Anomalous Small Angle X-ray Scattering (ASAXS)

Data acquisition and processing were carried out in the conditions detailed in a previous study [8], and based on the method developed by Humbert *et al.* [7] for CoMoS catalysts. In the present case, oxide catalyst precursor, catalysts at intermediate sulfidation temperatures and final catalysts were recorded in the same conditions. Quartz capillaries of 1.5 mm diameter were filled with pre-crushed samples in a glove box for the sulfided catalysts (*i.e.* all catalysts except A_D_ox and A_FD_ox catalysts precursors). Anomalous small-angle X-ray scattering experiments were performed on the D2AM beamline of the ESRF synchrotron. The scattered intensity was measured at five energies slightly below the molybdenum K-edge absorption, such as: E_1 (19700 eV), E_2 (19860 eV), E_3 (19940 eV), E_4 (19975 eV) and E_5 (19990 eV). The incident beam energy was calibrated with a metallic molybdenum foil. To cover the largest scattering vector q range, acquisitions were carried out at two sample-detector distances (35 mm and 3600 mm). The scattering images were recorded using a XPAD detector during 180 s to maximize the signal to noise ratio which is essential for the ASAXS signal discrimination of the particles and support. Since the porous support has a very strong SAXS signal, the photon collection rate can be very high, above the linearity range of the detector (and even high enough to damage the electronics). To stay within a reasonable counting rate close to the beam stop without compromising the data quality at high q, we used a semi-transparent beam stop composed of 2 copper square-shaped sheets of 50 µm thick which covered the first third of the q range approximately (in addition to a 2 mm led beam stop).

For 1D reduction, raw data were "flatfield" corrected to compensate the difference in efficiency of the detector pixels as well as our semi-transparent beamstop influence and normalized by i) the true thickness calculated from the transmission coefficient, ii) the incoming photon flux and iii) transmission. Intensity was calibrated by measuring a glassy carbon for both sample-to-detector distances at each energy. Intensity was expressed in absolute units, *i.e.* as the differential scattering cross section per unit volume in cm^{-1}.

The theoretical aspects of ASAXS technique are exhaustively described in Appendix E, only key information is detailed here. Considering a homogeneous matrix including randomly oriented particles with identical shape and with size parameterized by R, the SAXS scattered intensity $I(q)$ is expressed in Equation (1):

$$I(q) = \frac{N_p}{V_s} \Delta\rho^2 \int_0^\infty P(R)V(R)^2|F(q,R)|^2\Psi(q,R)dR \qquad (1)$$

where N_p the number of particles, V_s the sample volume, $P(R)$ the size distribution function, $V(R)$ the volume of the particles, $F(q,R)$ the form factor, $\Psi(q,R)$ the structure factor which equals to 1 when the particles are well dispersed, *i.e.* when distances

between particles are larger than particle sizes, and $\Delta\rho^2$ the contrast factor such as :

$$\Delta\rho^2 = \left(\rho_p - \rho_m\right)^2 \quad (2)$$

ρ_p and ρ_m the scattering length densities of the particles and the matrix:

$$\rho = r_e \sum_j n_j f_j \quad (3)$$

n_j the number density of the atom j in the matrix or in the particles, f_j the atomic form factors and r_e the classical Thomson radius (r_e = 0.282 10^{-12} cm). The term $\sum_j n_j f_j$ (e/Å^3) is defined as electronic density.

As a reminder, HDS catalysts are constituted of Mo containing particles supported on an oxide porous support such as alumina. It is impossible to discriminate the SAXS signal from the nanoparticles as the pores of support contribute significantly. Therefore, the ASAXS signal can be obtained by subtraction method [42–46]. By subtracting SAXS intensities from two different energies, the resulting intensity is only function of the Mo nanoparticles scattering as the contribution of the support is removed. Expression of ASAXS intensity from the Mo particles can be found in Equation (4).

$$\langle I(q,E_i)\rangle - \langle I\left(q,E_j\right)\rangle = n_p^2 r_e^2 \left(\left|f_p(E_i)\right|^2 - \left|f_p\left(E_j\right)\right|^2\right) \times \left(S_{pp}(q) + \alpha S_{sp}(q)\right) \quad (4)$$

where $\alpha = \frac{n_s f_s}{n_p \bar{f_p}}$ and $\bar{f_p} = \frac{f_p(E_i)+f_p(E_j)}{2}$ is the mean value of $f_p(E)$.

Considering independent Mo metallic particles of radius R_p deposited on support particles of radius R_s, it is possible to write $S_{pp}(q)$, and $S_{sp}(q)$ as follows:

$$S_{pp}(q) = \frac{N_p}{V_s} \int_0^{+\infty} P_p\left(R_p\right) V_p^2\left(R_p\right) F_p^2\left(q,R_p\right) dR_p \quad (5)$$

$$S_{sp}(q) = \frac{N_p}{V_s} \iint_0^{\infty} P_p(R_p) P_s(R_s) V_p(R_p) V_s(R_s) F_p(q,R_p) F_s(q,R_s) \frac{\sin\left(q\left(R_p+R_s\right)\right)}{q\left(R_p+R_s\right)} dR_p dR_s \quad (6)$$

In this context, $\alpha \approx 0.83$ so the interference term S_{sp} is probably not negligible. Both terms will be considered in the data modeling. A nonlinear least-squares adjustment of the ASAXS $I(E_i) - I(E_j)$ signal is performed on Equation (4) to evaluate the size distribution of the metallic nanoparticles. As seen in Figure 1, ASAXS $I(E_3) - I(E_5)$ curve of the A_D catalyst shows two inflections of the scattered signal. It induced the coexistence of molybdenum objects of two different sizes. At the smallest scattering vector q, the scattered intensity was attributed to a population of large Mo objects (*i.e.* aggregates of around several dozen of nm) modelled as ellipsoids of revolution (a spheroid) of axes R_a, R_a and νR_a with a form factor $F_{ellipsoid}\ (q,R_a,\nu)$ and a volume $V_a\ (R_a,\nu)$. Whereas at the highest scattering vector q, the signal was attributed to the presence of small Mo objects, *i.e.* Mo isolated/stacked slabs (*i.e.* around a few nm), modelled as discs of height $2H$ and radius R_p, with form factor $F_{disc}\ (q,R_p,H)$ and volume $V_p\ (R_p,H)$. The size distributions of these two populations were represented by log-normal distribution, as followed in equation (7):

$$P_k(R_k) = \frac{1}{\sqrt{2\pi}R_k\sigma_k} exp\left(-\frac{(ln\,R_k - \mu_k)^2}{2\sigma_k^2}\right) \quad (7)$$

where k equals to p for small Mo objects and to a for the bigger ones, and μ and σ are respectively the scale and the shape parameters of the lognormal law.

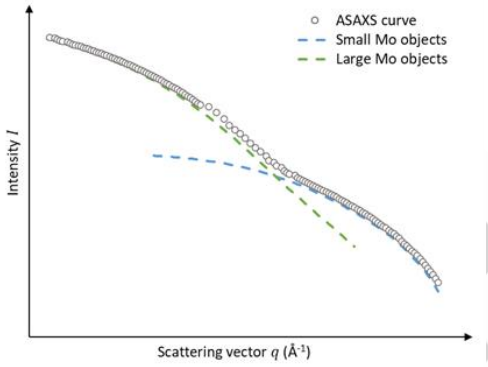

Figure 1. ASAXS $I(E_3) - I(E_5)$ curve processing of the A_D catalyst and multiscale Mo organization.

Finally, expression of ASAXS intensity from the Mo particles (*i.e.* both small (slabs) and large (aggregates) Mo objects) reported in Equation (4) can be expressed as the following **final model** (*cf.* Appendix E. for more details):

$$\langle I(q,E_i)\rangle - \langle I\left(q,E_j\right)\rangle = w_{Mo_x} * w_p * \frac{\rho_s}{\rho_{Mo_x}} * \Delta^2_{Mo_x}\left(E_i,E_j\right) \times \left(S'_{pp} + \alpha S'_{sp}\right) \quad (8)$$

with Mo_x = MoS_2 in the case of active phase, Mo_x = a*MoO_3 + b*MoS_x in the case of catalysts at intermediate sulfidation temperature and Mo_x = MoO_3 in the case of oxide molybdenum phase, ρ_{Mo_x} the density (g/cm^3) of the molybdenum phase, w_p and w_a are the fraction of molybdenum involved in the small or large Mo objects, respectively, and $\langle V_p\rangle$ and $\langle V_a\rangle$ are the mean volumes of the small and large Mo objects, w_{Mo_x} the weight concentration of the molybdenum phase (wt%), ρ_s the sample structural density (g/cm^3) and where:

$$\Delta^2_{Mo_x}\left(E_i,E_j\right) = {r_e}^2 * \left[\left(n_{Mo_x} f_{Mo_x}\left(E_i\right)\right)^2 - \left(n_{Mo_x} f_{Mo_x}\left(E_j\right)\right)^2\right] \quad (9)$$

$$S'_{pp}(q) = \left[\frac{1}{<V_p>}\int_0^{+\infty} P_p\left(R_p\right)\ V_p^2\left(R_p,H\right) F^2_{disc}\left(q,R_p,H\right) dR_p + \frac{w_a(1-\varepsilon_a)}{w_p} * \frac{1}{<V_a>}\int_0^{+\infty} P_a(R_a) V_a^2(R_a,\nu) F^2_{ellipsoid}(q,R_a,\nu)\, dR_a\right] \quad (10)$$

$$S'_{sp}(q) = \left[\frac{1}{<V_p>}\iint_0^{\infty} P_s(R_s) V_s(R_s) F_s(q,R_s) P_p(R_p) V_p\left(R_p,H\right) F_{disc}\left(q,R_p,H\right) \frac{sin\left(q\left(R_p+R_s\right)\right)}{q\left(R_p+R_s\right)} + \frac{w_a(1-\varepsilon_a)}{w_p} * \frac{1}{<V_a>}\iint_0^{\infty} P_s(R_s) V_s(R_s) F_s(q,R_s) P_a(R_a) V_a(R_a,\nu) F_{ellipsoid}(q,R_a,\nu) \frac{sin\left(q\left(R_a+R_s\right)\right)}{q\left(R_a+R_s\right)}\right] \quad (11)$$

with ε_a the porosity presents in the large Mo objects.

Thanks to this model, morphological information about those two populations were extracted. The main parameters are presented below, while an exhaustive list of all the parameters obtained is detailed in Appendix E.

Concerning the large molybdenum objects, one parameter was used to describe them:

- The mean width (*i.e.* diameter, in volume) W_{large} such as:

$$W_{large} = 2 * R_a \quad (12)$$

For the small molybdenum objects, two main parameters permitted to characterize them:

- The mean length L_{small} (in number) such as:

$$L_{small} = 2 * R_p \quad (13)$$

- The relative Mo amount (in %) involved in those small objects C_{small} such as:

$$C_{small} = (1 - \frac{w\varepsilon}{1+w\varepsilon}) * 100 \text{ and } w\varepsilon = \frac{w_a(1-\varepsilon_a)}{w_p} \quad (14)$$

Standard errors of ASAXS technique were evaluated and discussed in Appendix E. Relative uncertainties of L_{small}, W_{large} and C_{small} are about 29 %, 3 % and 1 % respectively.

Results

Oxide phase catalysts precursors description

EXAFS spectra of the Dried A_D_ox and Freeze-dried A_FD_ox catalysts precursors are plotted in Figure 2. The Mo speciation obtained from these EXAFS measurements by linear combination fitting of reference compounds (see experimental section) are reported in Figure 3. As a reminder, Mo species have been gathered into 4 categories (P-Heteropolyanions P-HPA, Polymolybdates PM, Monomolybdate MM and $AlMo_6$, cf Table 2). The amount of P-HPA is identical for both catalysts (*i.e.* 26 %)), but the freeze-dried A_FD_ox catalyst precursor presents at least twice more $AlMo_6$ species than the conventionally dried A_D_ox catalyst precursor (*i.e.* 37 % to 16 %). By compensation, the latter has much more polymolybdates species (*i.e.* 43 % to 28 %) and slightly more monomolybdates species (*i.e.* 15 % to 9 %). For detailed Mo speciation, see Figure A.1 (Supporting information).
EXAFS results have been consolidated with other characterization methods. **Raman spectroscopy** (see Figure B.1) has confirmed the presence of $AlMo_6$ in both catalysts. However, $AlMo_6$ was not observed by **XRD** (reported in Figure C.1) for both catalysts, highlighting the fact that this species is not well crystallized.
The important amount of $AlMo_6$ in the freeze-dried catalyst precursor, A_FD_ox can be explained by the freeze-drying protocol. During the ageing step, the impregnation solution is in contact with the γ-Al_2O_3 support and leads to the dissolution of the support. The release of Al^{3+} cations will form $AlMo_6$ Anderson HPA by complexation with polymolybdates [30, 33]. Right after ageing, the catalyst is frozen in liquid N_2 and then a freeze-drying consisting in solvent sublimation is applied which inhibits the redistribution of salts and solvent [47, 48]. We can hence consider that it freezes the state of the catalyst after ageing [8]. Conversely, preferential formation of polymolybdates occurs in the conventionally dried catalyst precursor, A_D_ox. This result is in line with the work of Barata et al. [33] where it was demonstrated that during the drying step, $AlMo_6$ species are consumed by reaction with monomolybdates MoO_4^{2-} to form polymolybdates for CoMoP/γ-Al_2O_3 catalysts with a P/Mo = 0.55 loaded with 8 wt% MoO_3. Even though the speciation of the dried catalyst is slightly different in the present work (P/Mo = 0.27, wt% MoO_3 = 26), the same reaction is probably occurring during drying.

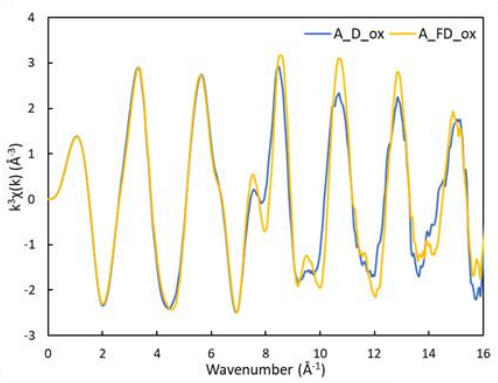

Figure 2. EXAFS curve of the A_D_ox and A_FD_ox catalysts precursors.

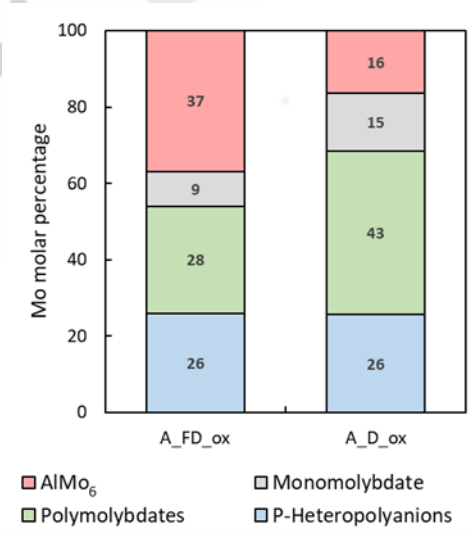

Figure 3. Mo speciation (EXAFS) of the A_D_ox & A_FD_ox catalysts precursors expressed as the Mo molar percentage.

ASAXS curves, plotted on Figure 4 and Figure 5 of the oxide catalyst precursors (dark blue curves), display only one inflection, around 8.10^{-2} $Å^{-1}$. It means that only one population is measurable in those catalysts by ASAXS. The ASAXS model presented in Equation (8) allows to obtain a data quantification. It considers the co-existence of two populations of different sizes but can also be applied for catalysts with only large Mo objects (*e.g.* both oxide catalysts, and both catalysts sulfided at 165°C), setting w_p = 0. Numerical values of the main morphological parameters obtained by ASAXS measurements are reported in Table 3. Aggregates are smaller in the dried catalyst precursor than in the freeze-dried,

with a mean aggregates width, W_{large}, of 9.9 and 15.5 nm respectively. Moreover, careful comparison of Mo aggregates size distributions of the oxide catalysts reported in Figure 6 shows that the A_FD_ox catalyst precursor has a larger distribution than the A_D_ ox catalyst: very small aggregates are present (W_{large} < 3 nm) as well as very large ones (W_{large} > 20 nm).

Furthermore, the presence of a peak at the highest q (*i.e.* at around q = 0.5 Å^{-1}) is noticed. It is representative of a periodic center-to-center distance d. The numerical value of this distance d is calculated with Equation (15):

$$d = \frac{2\pi}{q} \quad (15)$$

Distances d of 1.2 nm for the conventionally dried catalyst precursor A_D_ox and 1.3 nm for the freeze-dried catalyst precursor A_FD_ox are obtained and might indicate an organization between Mo oxide precursors. Indeed, these distance values are the same order of magnitude than the sizes of polymolybdates, $AlMo_6$ Anderson HPA and P-HPA sizes [49].

Table 3. Morphological information obtained by ASAXS measurements on the conventionally dried (A_D) and freeze-dried (A_FD) catalysts at each step of the sulfidation. d is the inter-object distance (nm) between the Mo oxide precursors, C_{small} is the relative Mo amount (%) involved in the small-size Mo objects, L_{small} (nm) is the mean length of the small-size Mo objects and W_{large} is the mean width (in surface, nm) of the large-size Mo objects.
*Relative uncertainties of C_{small}, L_{small}, W_{large} are about 1 %, 29 % and 3 % respectively.

Sample	Inter-object distance d (nm)	C_{small} (%)	L_{small} (nm)	W_{large} (nm)
A_D_ox	1.2	0	/	9.9
A_D_165	1.2	0	/	9.4
A_D_250	/	7	0.6	7.4
A_D_300	/	25	1.1	8.8
A_D_350	/	35	2.6	8.4
A_D	/	36	2.0	9.0
A_FD_ox	1.3	0	/	15.5
A_FD_165	/	0	/	6.6
A_FD_250	/	38	0.9	7.5
A_FD_300	/	40	1.2	7.9
A_FD_350	/	49	2.0	7.0
A_FD	/	31	1.7	9.1

Combining the following information: i) the oxide freeze-dried catalyst precursor A_FD_ox has twice more $AlMo_6$ than the oxide dried catalyst precursor A_D_ox, ii) the A_FD_ox catalyst precursor presents oxide aggregates larger than in the A_D_ox catalyst precursor and iii) P-HPA, PM and $AlMo_6$ seem to be close to each other and well-organized, as shown by the presence of a characteristic inter-objects distance d similar to their size; the assumption can been made **that oxide aggregates are composed of polymolybdates, $AlMo_6$ and P-HPA, while MoO_4^{2-} species are well dispersed within the support,** independently from the drying applied**.** Note that the presence of well-dispersed MoO_4^{2-} species can not be proved by ASAXS because of their small size and their low electronic density.

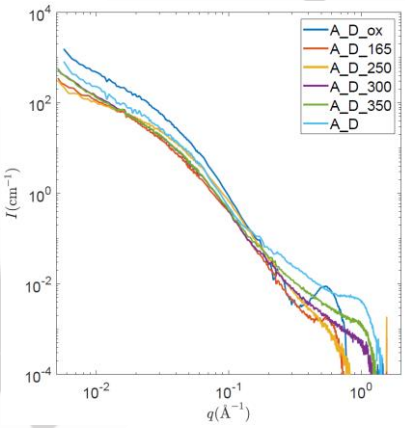

Figure 4. ASAXS curves of the conventionally dried catalysts depending of the sulfidation steps.

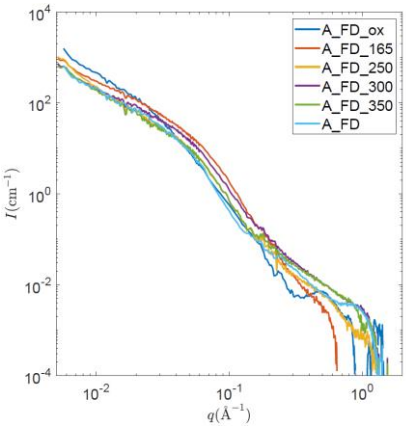

Figure 5. ASAXS curves of the freeze-dried catalysts depending of the sulfidation steps.

10.1002/cctc.202401670

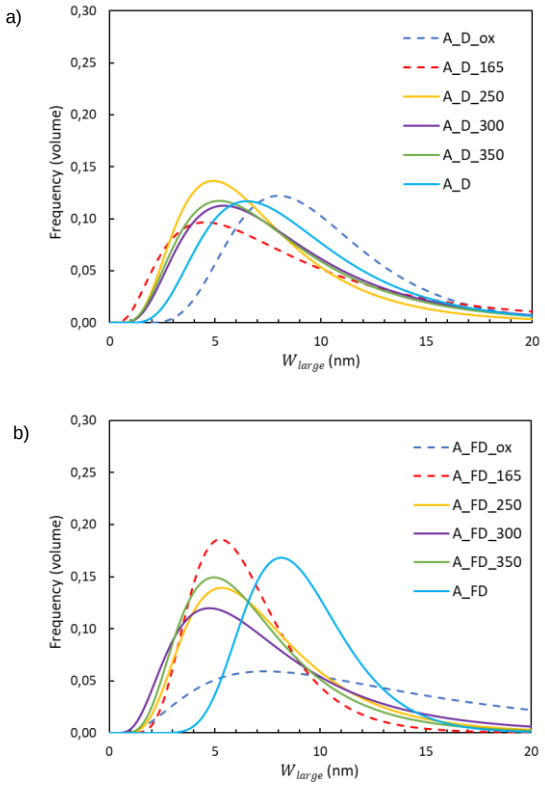

Figure 6. Mo aggregates size (W_{large}) distributions for the a) dried and b) freeze-dried catalysts during the sulfidation from ASAXS measurements.

Sulfide phase catalysts description

Catalysts after complete process of sulfidation (heating to 350°C and a 6 hours step), namely A_D and A_FD have been deeply characterized. XPS results (**Table 4**) show the same sulfidation rate (equal to 79%) for both catalysts, meaning that it remains 9 % of oxide Mo precursors (Mo(VI)) and 12 % of MoO_xS_y oxysulfides or MoS_3 species (Mo(V)). ASAXS characterization gives information on the multi-scale arrangement of the active phase (**Table 3**, Figure 4 and Figure 5). In both A_D and A_FD catalysts, slabs are highly aggregated with the proportion of Mo involved in small Mo objects, *i.e.* Mo isolated/stacked slabs (C_{small}) at only 36 and 31% respectively. They present the same mean size of aggregates (about 9 nm) but the size distribution is narrower in the freeze-dried sample with a maximum size near 9 nm compared to 7 nm in the conventionally dried one. Moreover Mo/Al measured by XPS is higher in the freeze-dried corresponding to a poorer dispersion of the active phase. Compared to oxide catalyst precursors, the aggregates in sulfide catalysts are much smaller, especially in catalyst A_FD. However, the size distribution of small Mo objects rise from 1 nm to 5 nm, with a mean length (L_{small}) of 2 nm in A_D and 1.7 nm in A_FD. Mo objects with L_{small} > 1 nm are naturally considered as MoS_2 slabs. Those < 1 nm correspond to Mo nanoclusters. Co-existence of these small Mo objects (MoS_2 slabs and nanoclusters) have been confirmed by **HR STEM-HAADF** image on the final A_D catalyst (see Figure 7). **HR STEM-HAADF** highlights the presence of slabs aggregates as well as stacked slabs. This stacking can be observed on the ASAXS curves of the final catalysts (see Figure 4 and Figure 5, light blue curves) which show a significant peak at q = 1 Å^{-1}.

However, the major differences observed in the oxide state between the two catalysts are not entirely preserved in the sulfide state, justifying the study of the evolution of Mo species organization during sulfidation. The catalysts were therefore characterized during activation, at different stages of the sulfidation temperature ramp.

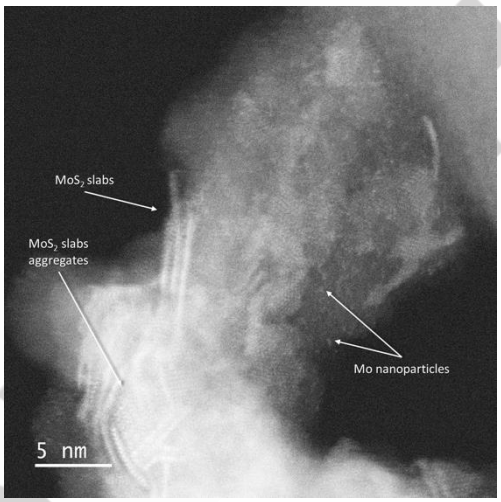

Figure 7. HR STEM-HAADF image of the dried and final catalyst A_D (after sulfidation stage).

Mo speciation and organization during sulfidation

XPS results of each sample (*i.e.* oxide catalyst precursors, catalysts at intermediate sulfidation temperatures and final catalysts) are reported below in Table 4. A comparison of speciation at each stage of the sulfidation shows that both catalysts follow the same evolution during activation. Evolution of Mo species proportion during sulfidation in the dried A_D catalyst is reported in Figure 8.

First, in the oxide catalyst precursor (*i.e.* A_D_ox), all the molybdenum precursors are under their oxide forms (% Mo(VI) = 100). Since the first sulfidation temperature (*i.e.* at 165°C), this amount decreases to finally reach 9 % Mo(VI) in the final catalyst. Above 165°C, Mo(V) species appears, usually attributed to oxysulfides or MoS_3 species. This means that the reduction and sulfidation have begun. However, it can be noted that this Mo(V) species reaches a maximum value of 23 % at 250°C and then decreases. In conjunction with the Mo(V) species decrease from 250°C, the Mo(IV) species attributed to MoS_2 emerges to reach *in fine* 79 % which corresponds to the $\%MoS_2$ sulfidation rate. Note that sulfidation is not fully complete once the final sulfidation temperature has been reached (*i.e.* at 350°C) since the sulfidation rate $\%MoS_2$ increases by 20 % during the sulfidation 6-h plateau. These results suggest a chain reaction during sulfidation: oxide species (Mo(VI)) are reduced and sulfided into either MoO_xS_y oxysulfides or MoS_3 species (Mo(V)), and finally transformed to

Table 4. XPS speciation of the cobalt, molybdenum, and sulfur species of the dried (A_D) and freeze-dried (A_FD) catalysts at each step.

Sample	Co relative atomic percentage			Mo relative atomic percentage			Atomic ratio
	Co^{2+}	CoS	CoMoS	Mo^{6+}	Mo^{5+}	Mo^{4+}	Mo/Al
A_D_ox	100	0	0	100	0	0	0.10
A_D_165	100	0	0	97	3	0	0.12
A_D_250	87	6	8	70	23	7	0.12
A_D_300	61	8	31	39	15	45	0.12
A_D_350	49	12	40	29	13	59	0.12
A_D	33	12	55	9	12	79	0.10
A_FD_ox	100	0	0	100	0	0	0.12
A_FD_165	100	0	0	98	2	0	0.15
A_FD_250	88	7	6	68	24	8	0.15
A_FD_300	62	8	30	38	18	43	0.15
A_FD_350	49	12	38	25	11	64	0.15
A_FD	39	11	51	9	12	79	0.12

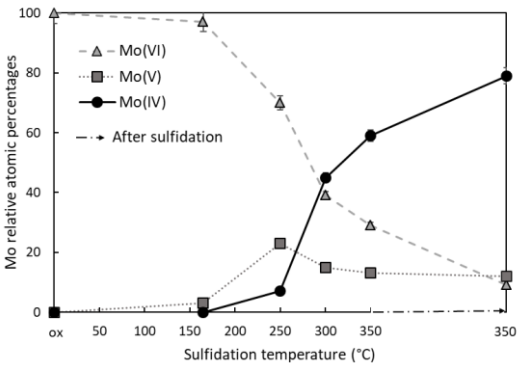

Figure 8. Evolution of the Mo relative atomic percentages of each species during the sulfidation of the dried A_D catalyst from XPS measurements.

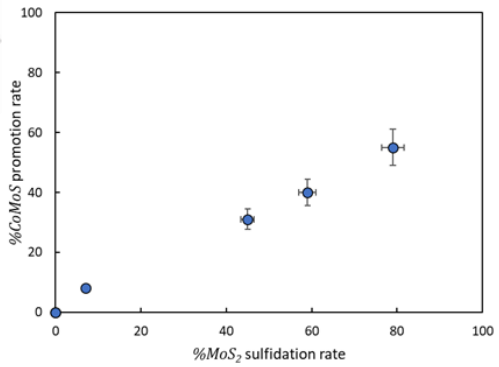

Figure 9. Evolution of the promotion rate %CoMoS (Co relative atomic percentage in CoMoS species) with the sulfidation rate %MoS_2 (Mo relative atomic percentage of MoS_2 species) during the sulfidation of the dried A_D catalyst from XPS measurements.

MoS_2 slabs (Mo(IV)), which is consistent with previous literature results [37]. However, not all species have been sulfided at the end of the sulfidation plateau since it remains 9 % of oxide Mo precursors and 12 % of oxysulfides or MoS_3 species.

In addition, Figure 9 reports that the MoS_2 promotion by cobalt (% CoMoS), and thus the formation of the CoMoS sites, occurs simultaneously with the Mo sulfidation (% MoS_2) and reaches a promotion rate $\%CoMoS$ of 55 % in the final catalyst A_D.

Figure 10 reports the evolution of the atomic ratio Mo/Al, which is linked to the Mo dispersion, for the 2 catalysts during sulfidation. For both catalysts, the same phenomenon occurs. There is a first step from the oxide catalyst to the one sulfided at 165°C where the Mo dispersion increases (*i.e.* Mo/Al increases). During all the sulfidation ramp, the Mo dispersion remains quite constant to finally decrease. Note that the freeze-dried catalyst has a better dispersion than the dried catalyst during all the sulfidation steps.

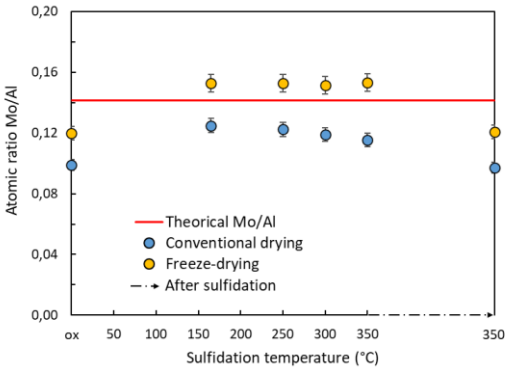

Figure 10. Evolution of the atomic ratio Mo/Al (XPS) of the dried and freeze-dried catalysts during sulfidation (theorical Mo/Al = 0.14).

To look at morphological changes, **ASAXS technique** was used. ASAXS curves are plotted on Figure 4 and Figure 5 respectively for the conventionally dried and freeze-dried catalysts. Each inflection present on ASAXS curves is attributed to a population differing by its size. As mentioned above, the curves of the oxide catalyst precursor (dark blue curves) and the sulfided catalyst at 165°C (red curves) display only one inflection, around 8.10^{-2} Å^{-1}. It means that only one population is measurable in those catalysts by ASAXS. However, above 250°C during the sulfidation, a second population appears as the ASAXS curves display now a second inflection at higher scattering vector q, which grows during sulfidation. The scattering vector being inversely proportional to object size, the first population found at the smallest scattering vector q is attributed to large Mo objects (around a dozen of nm). They may be aggregates of oxide precursors or aggregates of MoS_2 slabs, regarding the sulfidation state of the catalyst. The second type of Mo objects found at higher q, present only in sulfided catalysts is ascribed as MoS_2 either isolated or stacked (around a few nm), but also as Mo nanoclusters (smaller than 1 nm) as ASAXS can quantify this size of Mo objects [8].

The size distributions of these Mo populations are represented by log-normal distributions and are reported in Figure 6 for the size of Mo aggregates (W_{large}) and Figure 11 for the the mean length of the small-size Mo objects (L_{small} (nm)). The Mo aggregates size W_{large} distributions of the dried catalyst (see Figure 6 a)) show that, during the early stages of sulfidation, aggregates width is drastically reduced (dark blue and red dashed curves). Above 250°C, aggregates slightly grow and especially after a sulfidation plateau at 350°C (*i.e.* final catalyst; see light blue curve). Same patterns are observed in the freeze-dried catalyst (see Figure 6 b)) except that above 250°C the mean aggregates width remains constant and increases only during the last stage.

As mentioned before, a second population of small Mo objects appears at 250°C for both catalysts. At the beginning of the sulfidation (*i.e.* 250°C), most of the Mo objects are around 1 nm long and have been considered as Mo nanoparticles (with an unknown speciation). During the sulfidation, the mean length L_{small} increases similarly for both catalysts (voir figure 12a).

Relative amount of Mo involved in the small objects (*e.g.* C_{small}) can also be estimated by ASAXS for a simple chemical system, i.e. when molybdenum is fully oxidized or fully sulfided. However, for the catalysts at intermediate sulfidation temperatures A_D_x and A_FD_x, the system is more complex as a mixture of oxide, oxysulfide and sulfide species are present in the catalysts and makes it even more difficult to use C_{small} to describe quantitatively the aggregation state. Indeed, scattered intensity is function of the contrast factor of Mo objects and thus function of their oxidation state (see Equation (8)). Sulfide species are denser than oxide ones. This is why C_{small} is only an indicative parameter. Nevertheless, even taking this into account, both catalysts show two different behaviors (Figure 12b). For the freeze-dried, the relative amount of small objects remains almost constant from 250°C during all the sulfidation to finally decreases in the final catalyst (A_FD). To the contrary, for the dried A_D catalyst the relative amount of small Mo objects increases linearly during all the sulfidation process.

Discussion

By combining the results obtained from the different characterization techniques (EXAFS, ASAX and XPS) at each stage of the preparation of the catalyst (from drying to sulfidation) a complete scheme of the nucleation, growth and restructuration of the active phase can be proposed.

Early stage of the sulfidation process: oxide precursors depolymerization

At 165°C, sulfidation has not really started yet as DMDS fully decomposes into H_2S at around 230/250°C [37]. It is confirmed by XPS results reported in Table 4 as Mo species are still at 97 % under Mo^{6+} oxide form.
However, based on ASAXS and XPS results, the oxide phase morphology undergoes major changes as shown in **Figure 6** a) and b). Indeed, distributions of oxide aggregates width W_{large} drastically shifts to the lower values in both catalysts (dark blue and red dashed curves). In parallel, the Mo dispersion estimated with the atomic ratio Mo/Al increases (see Figure 10). Furthermore, there is a loss of the characteristic inter-objects distance d at 165°C in the Freeze-dried A_FD_165 catalyst but not in the Dried A_D_165 catalyst (see respectively Figure 5 and Figure 4).

Lesage et al. [37] have shown that when the sulfidation temperature rises but stays below 240°C, some of the initial oxide species disappear to reveal a second much smaller type of oxide objects, attributed to monomolybdates. Their formation could be explained by the dehydration or depolymerization of polyanions ($AlMo_6$, PM or P-HPA) into MoO_4^{2-} species. Moreover, Lesage et al. [29] evaluated the stability of Mo oxide precursors under H_2 reduction at 30 bar from RT to 250°C. They highlighted that Keggin P-HPA and most of PM are stable. However, $AlMo_6$ are unstable and depolymerize into MoO_4^2. The freeze-dried catalyst precursor A_FD_ox presents much more $AlMo_6$ species.

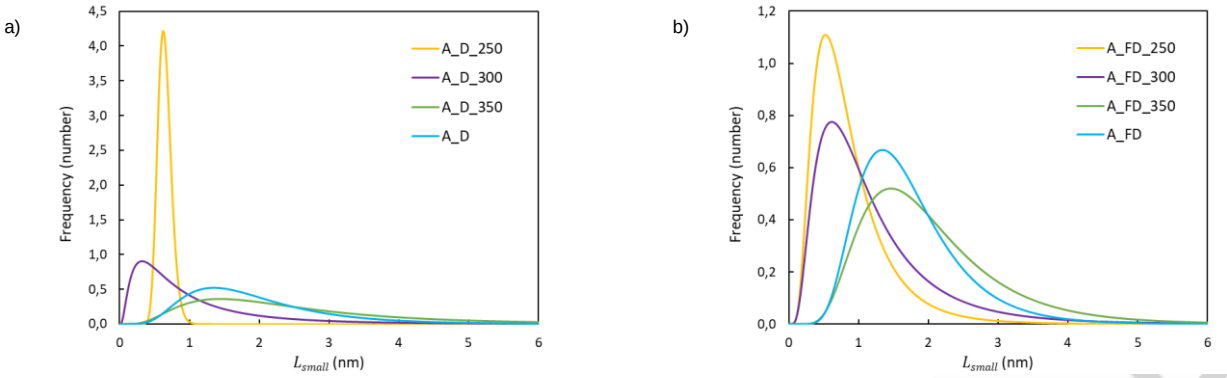

Figure 11. Slabs and nanoparticles size (L_{small}) distributions for the a) dried and b) freeze-dried catalysts during the sulfidation from ASAXS measurements.

Therefore, the loss of the characteristic inter-objects distance d at 165°C in A_FD_165 catalyst but not in A_D_165 catalyst suggests a lack of organization due to depolymerization of the $AlMo_6$ involved in the oxide aggregates, which could also explain the reduction in aggregate size. The loss of organization is slower for the dried A-D catalyst, since it is only observed at 250°C. This suggests that the P-HPA heteropolyanions undergo a second stage of modification at higher T°C. Aggregates can be seen as "reservoirs" for hyperdispersed MoO_4^{2-} species and their amount is expected to be higher in the freeze-dried catalyst. Thus, **below 240°C, part of the polymeric molybdenum species involved in the oxide Mo aggregates depolymerizes into MoO_4^{2-}**. In their work on the liquid-phase activation of CoMo-CA/Al_2O_3 catalysts followed by XAS/SAXS, Van Haandel et al. [39] did not observe such depolymerization phenomenon. As mentioned in the introduction, several differences can be raised between their systems and those presented in this work (*i.e.* nature of oxide precursors), but they also did not consider an aggregated Mo phase (*e.g.* oxide precursors aggregates or MoS_2 slabs aggregates). Consequently, they only follow the evolution from oxide to sulfide of well dispersed species.

Sulfidation: active phase nucleation and growth

Just before 250°C, catalysts are composed of well dispersed MoO_4^{2-} species and oxide aggregates mainly composed of PM and other polymeric molybdenum species. Moreover, it is supposed that the freeze-dried catalyst presents much more MoO_4^{2-} species than the dried catalyst due to massive $AlMo_6$ depolymerization. At 250°C, XPS measurements reported in Table 4 show the presence of Mo^{5+} attributed to oxysulfides or MoS_3 species and Mo^{4+} as MoS_2 active phase proving that sulfidation has started, which is consistent with decomposition temperature of DMDS to H_2S (240°C) [37]. Evolutions of the aggregates size (W_{large}) distributions reported respectively in **Figure 6** a) and b) show that, between 250°C and 350°C, W_{large} increases slightly in the dried catalyst while it remains constant in the freeze-dried one.

At 250°C, a second population composed of small Mo objects (*i.e.* less than 5 nm) starts to be measured in ASAXS (Figure 12 a) and b) respectively). In agreement with XPS results, this small population of Mo objects can be attributed to either oxysulfides and/or MoS_3, MoS_2 nuclei or even MoS_2 slabs. Electronic densification, and thus the increase of the electronic density, as well as particles growth, now make these small Mo objects visible in ASAXS. As the relative amount of this population C_{small} at 250°C is more than five times higher in the freeze-dried catalyst than in the dried catalyst (C_{small}{A_FD_250} = 38 % and C_{small}{A_D_250} = 7 %), the assumption can be made that small dispersed monomolybdates species sulfide more easily than oxide aggregates. Size distributions L_{small} reported in Figure 11 of the A_FD_250 (yellow curve) also highlights the advanced sulfidation of the smallest Mo objects in the freeze-dried catalyst as it shows Mo nanoparticles (L_{small} < 1 nm), but also well formed MoS_2 slabs (1 nm < L_{small} < 5 nm), while the A_D_250 catalyst only displays the smallest Mo nanoparticles. Combination of XPS and ASAXS techniques allows to discuss about the nature of less than 1 nm Mo nanoparticles. As these objects appear with the sulfidation, their oxidation state must be Mo(V): it could either be MoO_xS_y or MoS_3 which are transient species before MoS_2 slabs formation [12, 13, 50]. Those objects could also be under the Mo(IV) form and might be MoS_2 nuclei in growth process. In the case of van Haandel et al. [39], they did not observe the formation of MoS_x intermediate species but a direct crystallization and growth of MoS_2 stacked slabs from the oxide precursors.

As a reminder, XPS has showed that sulfidation rates are quite identical during each step of the sulfidation for both catalysts. Even if MoO_4^{2-} species are preferentially sulfided, there is less monomolybdates in the dried catalyst compared to the supplied sulfur amount. Thus, oxide aggregates constituted of polymeric molybdenum species could be sulfided in parallel which agrees with both W_{large} and C_{small} increase in the dried catalyst, while it remains constant in the freeze-dried between 250°C and 350°C.

Therefore, **dispersed MoO_4^{2-} particles appears to be** preferentially sulfided. **In the freeze-dried catalyst, the high MoO_4^{2-} amount is sufficiently high to be the main species sulfided**. **Sulfidation of MoO_4^{2-} leads to the formation of Mo nanoparticles mixture of Mo^{V} and Mo^{VI}, which will generate the dispersed MoS_2 phase nucleation and growth. However, in the dried catalyst there is less MoO_4^{2-} species, so both well dispersed MoO_4^{2-} and oxide aggregates constituted of polymeric molybdenum species are sulfided in parallel.**

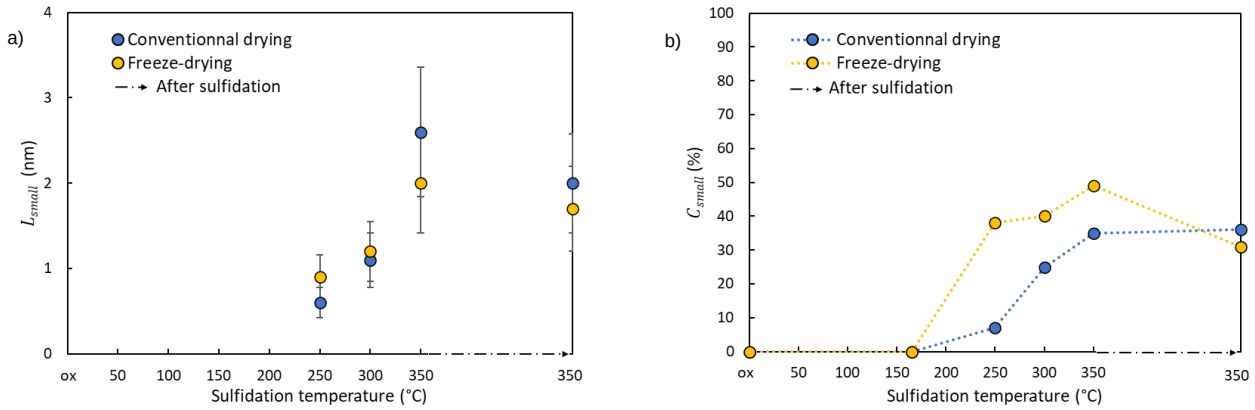

Figure 12. Evolution of a) mean small Mo objects length (L_{small}) and b) the relative amount of Mo involved in small objects (C_{small}) for conventionally dried and freeze-dried catalysts during the sulfidation from ASAXS measurements.

Active phase restructuration

Once the sulfidation temperature has reached 350°C, a 6-h plateau is applied. It leads to a drastic increase of the sulfidation rate for both catalysts: from 59 and 64 % to 79 %. Note that for both catalysts, 9 % of Mo(VI) oxides and 12 % of Mo(V) oxysulfides remain, as previously reported for such catalysts. Besides, the presence of multiscale Mo organization such as MoS_2 slabs and slabs aggregates have been confirmed by HR STEM-HAADF image of the A_D catalyst reported in Figure 7. This image highlights also the presence of Mo nanoparticles with sizes below 1 nm in agreement with ASAXS slabs length distributions of the dried and freeze-dried final catalysts (see Figure 11 a) and b), light blue curves). These Mo nanoparticles could either be oxysulfides particles or MoS_x nanoclusters as observed by Ryaboshapka et al [11] on Mo/Al_2O_3 catalysts prepared from $(NH_4)_6Mo_7O_{24}.4H_2O$ (AHM).

Significative changes occur during this step. Indeed, a decrease of the relative small Mo objects amount C_{small} in the freeze-dried catalyst (from 49 % to 31 %, as seen in Figure 12 b)) and an increase of the mean aggregate width W_{large} for both catalysts (**Figure 6**), which is even more pronounced for the freeze-dried catalyst.

It has been assumed above that sulfidation of **oxide aggregates is delayed compared to MoO_4^{2-} in the freeze-dried catalyst. Thus, during the sulfidation stage, the only remaining species to be sulfided are the oxide aggregates**. As explained previously, C_{small} parameter is a function of the relative proportion of large aggregates and small dispersed objects, but it is also a function of the metallic particles electronic density. Consequently, if oxide aggregates are sulfided during the 350°C plateau, the C_{small} parameter could decrease not because of an aggregation phenomenon, but because the electronic density, and thus the contrast factor, of molybdenum species involved in aggregates has radically increased. This phenomenon is less pronounced in the conventionally dried catalyst, due to a simultaneous sulfidation of monomolybdates and oxide aggregates occurring earlier as proposed previously.

Similarly, aggregate width W_{large} increases constantly during the sulfidation ramp and during the 350°C plateau as seen on the Mo aggregates size distribution of the dried catalyst (A_D) reported in **Figure 6** a). Conversely, W_{large} remains constant during the sulfidation ramp for the freeze-dried catalyst (A_FD, see **Figure 6** b), and suddenly increases for the final catalyst A_FD with a final aggregate width of 9.1 nm. It is consistent with the loss of Mo dispersion observed in the final catalysts by XPS measurements as seen in Figure 10. During sulfidation, mobile Mo species such as MoO_xS_y or MoS_2 nuclei probably coalesce together to form MoS_2 slabs. On ASAXS curves for both final catalysts (*i.e.* A_ D and A_FD), a peak is observable at around 1 $Å^{-1}$, suggesting a stacking phenomenon. Moreover, an expansion of aggregates sizes W_{large} is seen during sulfidation through ASAXS measurements. These observations lead to the following assumption: **MoS_2 formation associated to coalescence of Mo species and stacking within the aggregates induces an organizational restructuration. This rearrangement creates porosity and drives the expansion of the aggregate's width**.

A summary of the hypothesis about the genesis of the multiscale active phase is given in Scheme 1.

.

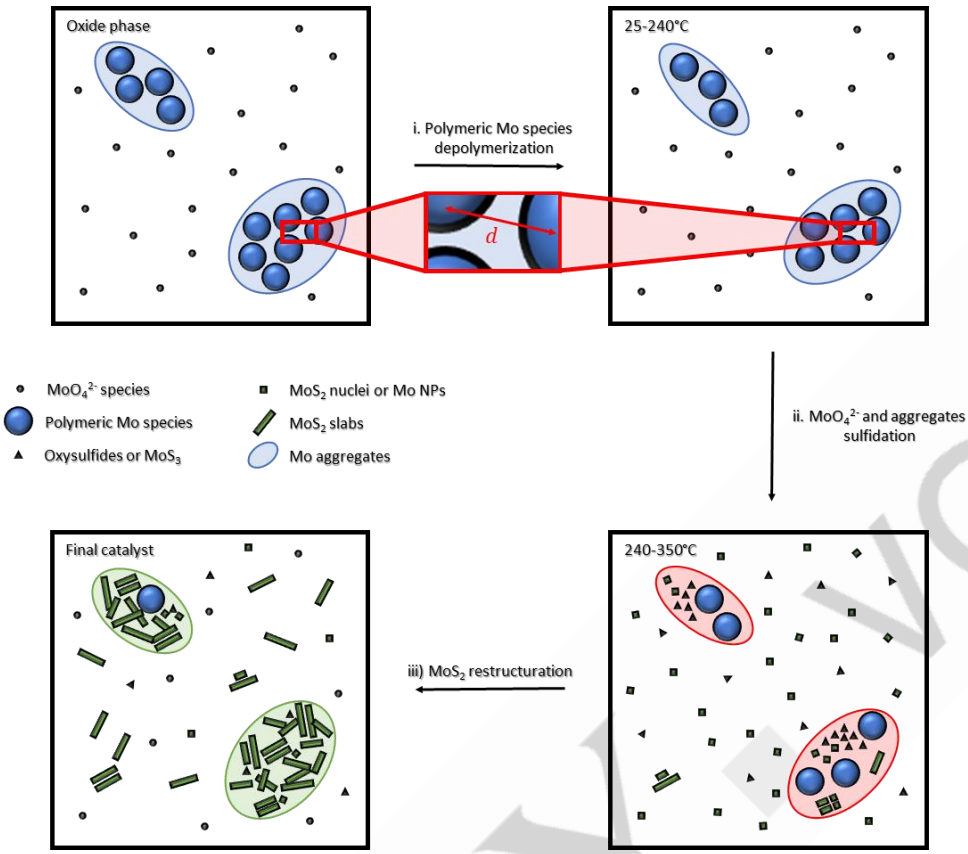

Scheme 1. Schematic representation of the genesis of the Mo multiscale organization within the conventionnally dried catalyst from oxide to sulfide.

Mechanism of a nucleation and growth of MoS_2 slabs has not yet been discussed. Several mechanisms of MoS_2 slabs formation can be considered as explained earlier, such as: layer-and-layer, layer-by-layer, and either layer-on-layer as proposed before by Hansen et al. [38]. These authors showed with *in-situ* TEM that stacked MoS_2 slabs are formed layer-by-layer: a new slab could be nucleated and grow on the top of an already existing mono-slab. Stacking would be favored by an important local Mo loading. However, van Haandel et al [39], in their XAS/SAXS combined study, explained the MoS_2 active phase formation by coalescence of MoS_x species due to their proximity which could correspond to a layer-and-layer mechanism following the definition of Hansen et al. [38] (*i.e.* simultaneous growth of the layers present in stacked slabs). Different mechanisms could thus coexist. It can be proposed that isolated and stacked slabs resulting from the sulfidation of well dispersed MoO_4^{2-} species are more likely to be formed through the layer-by-layer mechanism. Conversely, inside the aggregates, due to the high concentration and proximity of Mo atoms, the slab formation could occur through a layer-and-layer mechanism.

Conclusion

This work brings new insights on the genesis of the multiscale molybdenum organization, from synthesis (*i.e.* oxide phase) to sulfidation. Combination of EXAFS and ASAXS techniques shows that oxide catalysts are composed of both dispersed MoO_4^{2-} and oxide aggregates of P-HPA (P-heterepolyanions), polymolybdates and $AlMo_6$. Comparing the behaviors of dried and freeze-dried catalysts with XPS and ASAXS techniques during sulfidation permit to deduce a common 3-steps mechanism in the multiscale active phase organization:

i) from RT to 240°C (i.e. the sulfiding agent has not yet decomposed into H_2S), polymeric molybdenum species presents in oxide aggregates depolymerizes into monomolybdates MoO_4^{2-} entities well dispersed on the support;

ii) these small entities are preferentially sulfided compared to oxide aggregates. In case of important amount of MoO_4^{2-}, the sulfidation of oxide aggregates is delayed;

iii) during aggregates sulfidation, a restructuration is observed. Mo precursors contained in oxide aggregates condense by sulfidation. Mobility of these species leads to a size expansion of the sulfide aggregates which induces porosity in the MoS_2 slab aggregates.

Even if the proposed mechanism is the same for both catalysts, kinetics of these steps is influenced by their initial composition (*i.e.* oxide phase speciation). In the freeze-dried catalyst, the system has been frozen after impregnation and ageing where high amounts of $AlMo_6$, formed by support dissolution, are observed and leads to large Mo oxide aggregates. Conversely, in the dried catalyst, $AlMo_6$ species are consumed to form polymolybdates during drying. In the freeze-dried catalyst, $AlMo_6$ and P-HPA depolymerization produces numerous dispersed MoO_4^{2-}. As monomolybdates are preferentially sulfided, sulfidation of the

oxide aggregates in the freeze-dried catalyst is delayed, leading to bigger slabs aggregates than in the dried catalyst due to active phase restructuration. The initial properties of the catalysts in the oxide state therefore appear to determine the final multiscale Mo organization and are likely to influence catalytic performances *in fine*. As preparation modes have a real influence on oxide and consequently sulfide organizations, it could be interesting to corroborate those observations with other synthesis parameters (*e.g.* additivation, drying severity, etc).

Supporting Information

The authors have cited additional references within the Supporting Information.

Acknowledgements

EXAFS measurements were carried out on ROCK beamline at the SOLEIL synchrotron. We are grateful to Dr Valérie Briois for the beamtime allocated. ASAXS experiments were performed on BM02-CRG beamline at the ESRF. We are grateful to the beamline staff for smoothly running the facility. We would like to also thank Saloua Sahal-El Ahrache and Anne-Lise Taleb for the XPS and HR-STEM HAADF analysis.

Keywords: Hydrodesulfurization • CoMoP/Al_2O_3 • Active phase organization • ASAXS • genesis

[1] *iea*. https://www.iea.org/reports/world-energy-outlook-2022/executive-summary.
[2] Breysse, M.; Geantet, C.; Afanasiev, P.; Blanchard, J.; Vrinat, M. *Catalysis Today* **2008**, *130*, 3–13.
[3] Topsøe, H. *Applied Catalysis A: General* **2007**, *322*, 3–8. https://doi.org/10.1016/j.apcata.2007.01.002.
[4] Topsøe, H.; Clausen, B. S.; Candia, R.; Wivel, C.; Mørup, S. *Journal of Catalysis* **1981**, *68*, 433–452.
[5] Lauritsen, J. V.; Bollinger, M. V.; Lægsgaard, E.; Jacobsen, K. W.; Nørskov, J. K.; Clausen, B. S.; Topsøe, H.; Besenbacher, F. *Journal of Catalysis* **2004**, *221* (2), 510–522. https://doi.org/10.1016/j.jcat.2003.09.015.
[6] Toulhoat, H.; Raybaud, P. *Catalysis by Transition Metal Disulphides: Atomic Scale Structure of Mixed Lamellar Sulphides*; Technip: Paris, France, 2013.
[7] Humbert, S.; Devers, E.; Lesage, C.; Legens, C.; Lemaitre, L.; Sorbier, L.; De Geuser, F.; Briois, V. *Journal of Catalysis* **2021**, *395*, 412–424. https://doi.org/10.1016/j.jcat.2021.01.033.
[8] Cottrez, C.; Humbert, S.; Gay, A.; Devers, E.; De Geuser, F.; Carrier, X.; Chaumonnot, A. *ChemCatChem* **2023**, *15* (6), e202201432. https://doi.org/10.1002/cctc.202201432.
[9] Baubet, B.; Girleanu, M.; Gay, A.-S.; Taleb, A.-L.; Moreaud, M.; Wahl, F.; Delattre, V.; Devers, E.; Hugon, A.; Ersen, O.; Afanasiev, P.; Raybaud, P. *ACS Catal.* **2016**, *6* (2), 1081–1092. https://doi.org/10.1021/acscatal.5b02628.
[10] Ryaboshapka, D.; Piccolo, L.; Aouine, M.; Bargiela, P.; Briois, V.; Afanasiev, P. *Applied Catalysis B: Environmental* **2022**, *302*, 120831. https://doi.org/10.1016/j.apcatb.2021.120831.
[11] Ryaboshapka, D.; Len, T.; Bargiela, P.; Aouine, M.; Geantet, C.; Briois, V.; Piccolo, L.; Afanasiev, P. *ACS Catal.* **2023**, *13* (15), 10511–10526. https://doi.org/10.1021/acscatal.3c01672.
[12] Payen, E.; Kasztelan, S.; Houssenbay, S.; Szymanski, R.; Grimblot, J. *J. Phys. Chem.* **1989**, *93* (17), 6501–6506. https://doi.org/10.1021/j100354a043.
[13] Rochet, A.; Baubet, B.; Moizan, V.; Pichon, C.; Briois, V. *Comptes Rendus. Chimie* **2016**, *19* (10), 1337–1351. https://doi.org/10.1016/j.crci.2016.01.009.
[14] Munnik, P.; De Jongh, P. E.; De Jong, K. P. *Chem. Rev.* **2015**, *115* (14), 6687–6718. https://doi.org/10.1021/cr500486u.
[15] Garcia De Castro, R.; Devers, E.; Digne, M.; Lamic-Humblot, A.-F.; Pirngruber, G. D.; Carrier, X. *Journal of Catalysis* **2021**, *403*, 16–31. https://doi.org/10.1016/j.jcat.2021.01.026.
[16] Dominguez Garcia, E.; Chen, J.; Oliviero, E.; Oliviero, L.; Maugé, F. *Applied Catalysis B: Environmental* **2020**, *260*, 117975. https://doi.org/10.1016/j.apcatb.2019.117975.
[17] Zhou, W.; Yang, L.; Liu, L.; Chen, Z.; Zhou, A.; Zhang, Y.; He, X.; Shi, F.; Zhao, Z. *Applied Catalysis B: Environmental* **2020**, *268*, 118428. https://doi.org/10.1016/j.apcatb.2019.118428.
[18] Zhang, D.; Liu, X.-M.; Liu, Y.-X.; Yan, Z.-F. *Microporous and Mesoporous Materials* **2021**, *310*, 110637. https://doi.org/10.1016/j.micromeso.2020.110637.
[19] Chen, W.; Nie, H.; Long, X.; Li, M.; Zhang, L.; Li, D. *Catalysis Today* **2021**, *377*, 69–81. https://doi.org/10.1016/j.cattod.2020.07.043.
[20] Prada Silvy, R. *Catalysis Today* **2019**, *338*, 93–99. https://doi.org/10.1016/j.cattod.2019.07.013.
[21] Le Bihan, L.; Blanchard, P.; Fournier, M.; Grimblot, J.; Payen, E. *Faraday Trans.* **1998**, *94* (7), 937. https://doi.org/10.1039/a706359h.
[22] Blanchard, P.; Lamonier, C.; Griboval, A.; Payen, E. *Applied Catalysis A: General* **2007**, *322*, 33–45. https://doi.org/10.1016/j.apcata.2007.01.018.
[23] Platanitis, P.; Panagiotou, G. D.; Bourikas, K.; Kordulis, C.; Fierro, J. L. G.; Lycourghiotis, A. *Journal of Molecular Catalysis A: Chemical* **2016**, *412*, 1–12. https://doi.org/10.1016/j.molcata.2015.11.012.
[24] Nikulshina, M.; Kokliukhin, A.; Mozhaev, A.; Nikulshin, P. *Catalysis Communications* **2019**, *127*, 51–57. https://doi.org/10.1016/j.catcom.2019.05.003.
[25] Afanasiev, P. *Applied Catalysis A: General* **2017**, *529*, 10–19. https://doi.org/10.1016/j.apcata.2016.10.008.
[26] Bergwerff, J. A.; Van De Water, L. G. A.; Visser, T.; De Peinder, P.; Leliveld, B. R. G.; De Jong, K. P.; Weckhuysen, B. M. *Chemistry A European J* **2005**, *11* (16), 4591–4601. https://doi.org/10.1002/chem.200500116.
[27] Bergwerff, J. A.; Jansen, M.; Leliveld, B. (R.) G.; Visser, T.; De Jong, K. P.; Weckhuysen, B. M. *Journal of Catalysis* **2006**, *243* (2), 292–302. https://doi.org/10.1016/j.jcat.2006.07.022.
[28] Griboval, A.; Blanchard, P.; Payen, E.; Fournier, M.; Dubois, J. L. Alumina Supported HDS Catalysts Prepared by Impregnation with Newheteropolycompounds. In *Studies in Surface Science and Catalysis*; Elsevier, 1997; Vol. 106, pp 181–194. https://doi.org/10.1016/S0167-2991(97)80016-X.
[29] Lesage, C. Caractérisation Par Quick-XAS Operando Du Rôle de l'additif Organique Sur Le Mécanisme de Sulfuration En Phase Liquide Des Catalyseurs d'hydrotraitement, Université Paris-Sud, 2019.
[30] Carrier, X.; Lambert, J.-F.; Kuba, S.; Knözinger, H.; Che, M. *Journal of Molecular Structure* **2003**, *656* (1–3), 231–238. https://doi.org/10.1016/S0022-2860(03)00328-4.
[31] Al-Zeghayer, Y. S.; Sunderland, P.; Al-Masry, W.; Al-Mubaddel, F.; Ibrahim, A. A.; Bhartiya, B. K.; Jibril, B. Y. *Applied Catalysis A: General* **2005**, *282* (1–2), 163–171. https://doi.org/10.1016/j.apcata.2004.12.021.
[32] Munnik, P.; Krans, N. A.; De Jongh, P. E.; De Jong, K. P. *ACS Catal.* **2014**, *4* (9), 3219–3226. https://doi.org/10.1021/cs5006772.
[33] Barata, B.; Legens, C.; Devers, E.; Delpoux, O.; Barthe, L.; Roudenko, O.; Briois, V. *ChemCatChem* **2023**, *15* (7), e202201440. https://doi.org/10.1002/cctc.202201440.
[34] Schrader, G. L.; Cheng, C. P. *Journal of Catalysis* **1983**, *80* (2), 369–385. https://doi.org/10.1016/0021-9517(83)90262-2.

[35] De Jong, A. M.; Borg, H. J.; van Ijzendoorn, L. J.; Soudant, V. G. F. M.; De Beer, V. H. J.; Van Veen, J. A. R.; Niemantsverdriet, J. W. *J. Phys. Chem.* **1993**, *97* (24), 6477–6483.
[36] Muijsers, J. C.; Weber, Th.; van Hardeveld, R. M.; Zandbergen, H. W.; Niemantsverdriet, J. W. *Journal of Catalysis* **1995**, *157* (2), 698–705.
[37] Lesage, C.; Devers, E.; Legens, C.; Fernandes, G.; Roudenko, O.; Briois, V. *Catalysis Today* **2019**, *336*, 63–73. https://doi.org/10.1016/j.cattod.2019.01.081.
[38] Hansen, L. P.; Johnson, E.; Brorson, M.; Helveg, S. *J. Phys. Chem. C* **2014**, *118* (39), 22768–22773. https://doi.org/10.1021/jp5069279.
[39] Van Haandel, L.; Longo, A.; Bras, W.; Hensen, E. J. M.; Weber, T. *ChemCatChem* **2019**, *11* (20), 5013–5017. https://doi.org/10.1002/cctc.201901390.
[40] Gandubert, A. D.; Legens, C.; Guillaume, D.; Rebours, S.; Payen, E. *Oil & Gas Science and Technology - Rev. IFP* **2007**, *62* (1), 79–89. https://doi.org/10.2516/ogst:2007007.
[41] *plugim*. https://www.plugim.fr/.
[42] Haubold, H.-G.; Wang, X. H. *Nuclear Instruments and Methods in Physics Research Section B: Beam Interactions with Materials and Atoms* **1995**, *97* (1–4), 50–54. https://doi.org/10.1016/0168-583X(95)00200-6.
[43] Haubold, H.-G.; Wang, X. H.; Jungbluth, H.; Goerigk, G.; Schilling, W. *Journal of Molecular Structure* **1996**, *383* (1–3), 283–289. https://doi.org/10.1016/S0022-2860(96)09300-3.
[44] Haubold, H.-G.; Wang, X. H.; Goerigk, G.; Schilling, W. *J Appl Crystallogr* **1997**, *30* (5), 653–658. https://doi.org/10.1107/S0021889897002422.
[45] Haubold, H.-G.; Vad, T.; Waldöfner, N.; Bönnemann, H. *J Appl Crystallogr* **2003**, *36* (3), 617–620. https://doi.org/10.1107/S0021889803005144.
[46] Wen, F.; Waldöfner, N.; Schmidt, W.; Angermund, K.; Bönnemann, H.; Modrow, S.; Zinoveva, S.; Modrow, H.; Hormes, J.; Beuermann, L.; Rudenkiy, S.; Maus-Friedrichs, W.; Kempter, V.; Vad, T.; Haubold, H. *Eur J Inorg Chem* **2005**, *2005* (18), 3625–3640. https://doi.org/10.1002/ejic.200500446.
[47] Eggenhuisen, T. M.; Friedrich, H.; Nudelman, F.; Zečević, J.; Sommerdijk, N. A. J. M.; De Jongh, P. E.; De Jong, K. P. *Chem. Mater.* **2013**, *25* (6), 890–896. https://doi.org/10.1021/cm3037845.
[48] Eggenhuisen, T. M.; Munnik, P.; Talsma, H.; De Jongh, P. E.; De Jong, K. P. *Journal of Catalysis* **2013**, *297*, 306–313. https://doi.org/10.1016/j.jcat.2012.10.024.
[49] Surman, A. J.; Robbins, P. J.; Ujma, J.; Zheng, Q.; Barran, Perdita. E.; Cronin, L. *J. Am. Chem. Soc.* **2016**, *138* (11), 3824–3830. https://doi.org/10.1021/jacs.6b00070.
[50] Weber, Th.; Muijsers, J. C.; Van Wolput, J. H. M. C.; Verhagen, C. P. J.; Niemantsverdriet, J. W. *J. Phys. Chem.* **1996**, *100* (33), 14144–14150. https://doi.org/10.1021/jp961204y.

10.1002/cctc.202401670

WILEY VCH

RESEARCH ARTICLE

Entry for the Table of Contents

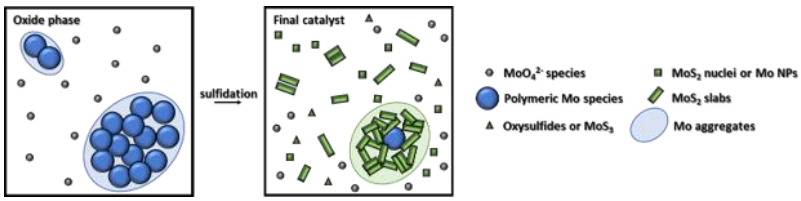

The genesis of the multiscale MoS_2 organization followed by ASAXS (Anomalous Small Angle X-Ray-Scattering) and XPS shows a 3-steps genesis: i) a depolymerization of $AlMo_6$ into MoO_4^{2-}, ii) a preferential sulfidation of the well-dispersed species (*i.e.* MoO_4^{2-}) into MoS_2, and iii) a final restructuration of the slabs within the aggregates. Synthesis parameters are key to drive the sulfide organization.